Large-pore mesoporous RuNi-doped TiO_2–Al_2O_3 nanocomposites for highly efficient selective CO methanation in hydrogen-rich reformate gases

Xiaoping Dai [a,*], Ji Liang [b], Ding Ma [c], Xin Zhang [a], Huabo Zhao [c], Bo Zhao [c], Zhenguo Guo [a], Freddy Kleitz [d], Shizhang Qiao [b,**]

[a] State Key Laboratory of Heavy Oil Processing, China University of Petroleum, Beijing 102249, China
[b] School of Chemical Engineering, The University of Adelaide, Adelaide, SA 5005, Australia
[c] College of Chemistry and Molecular Engineering, Peking University, Beijing 100871, China
[d] Department of Chemistry, Université Laval, Quebec G1V 0A6, QC, Canada

ARTICLE INFO

ABSTRACT

A series of large-pore mesoporous RuNi-doped TiO_2–Al_2O_3 nanocomposites were prepared by a facile sol–gel method using a one-pot protocol based on evaporation-induced self-assembly. Owing to high density of active sites, an open nanoarchitecture and highly promotional efficiency by synergetic effects, the as-prepared nanocomposites demonstrated excellent catalytic properties in selective CO methanation (CO-SMET). The final concentration of CO can be reduced to less than 50 ppm with more than 50% selectivity over the MRNAT-30Ni catalyst. The working temperature window covered the typical working range of 200–250 °C in conventional upstream low-temperature shift reactors. The MRNAT-30Ni catalyst has excellent stability during 200 h time on stream with no detectable change in CO and CH_4 concentrations, and CO in outlet reaches level below 20 ppm under realistic reaction conditions. This remarkable improvement of activity/selectivity and stability could lead to wide implementation of this one-pot protocol for the synthesis of large-pore mesoporous nanocomposite catalysts for the CO-SMET process.

© 2014 Elsevier B.V. All rights reserved.

1. Introduction

Hydrogen (H) is one of the most abundant elements on earth, and H_2 can be produced from renewable energy sources; thus, it represents an important alternative to current fossil energy. Generally, H_2 used in a fuel cell is mainly produced through a multistep process, including catalytic reforming of hydrocarbons followed by a water gas shift (WGS). A major issue is the production of ~1% carbon monoxide (CO) in the reformate gas from WGS, which make CO concentration much higher than the maximum permitted CO concentration (max. 10 ppm for Pt electrodes, and 50 ppm for Pt-alloy electrodes) to avoid poisoning of the fuel cell catalysts [1–7]. Various approaches have been proposed to reduce CO concentration

in H_2, such as preferential oxidation of CO (PROX) [8–12], membrane separation of CO from H_2 [13] and selective methanation of CO (CO-SMET) [1–5,14]. However, the high cost and high-pressure operation of a membrane separation method, and additional monitoring and units for O_2 dosing, and additional maintenance of the PROX process make it limited in cost sensitive, small scale applications (such as block heating stations). Thus, direct methanation of CO to form methane and water has been studied as an alternative owing to its many advantages such as independence of oxygen/air, the reusability of the resultant methane, and very small actual energy loss in the fuel cell [1,5,15]. High selectivity in CO-SMET process is a critical requirement for methanation catalysts to avoid excessive heat production, which is formed during the uncontrolled exothermic CO_2 methanation, resulting ultimately in the catalyst deactivation. Evidently, it still remains a great challenge to suppress the simultaneous methanation of CO_2 in H_2-rich reformate gases (ca. 20 vol% CO_2). Otherwise the losses of hydrogen would become intolerable [16]. In addition, the reverse water gas shift (RWGS) reaction often occurs at low space velocities or high reaction temperature, which can convert CO_2 to CO, making it more difficult to achieve acceptable CO concentrations [16].

* Corresponding author at: School of Chemical Engineering, The University of Adelaide, Adelaide, SA 5005, Australia. Tel.: +61 8 8313 6443; fax: +61 8 8313 4373.
** Corresponding author at: State Key Laboratory of Heavy Oil Processing, China University of Petroleum, Beijing 102249, PR China. Tel.: +86 10 89734979; fax: +86 10 89734979.
E-mail addresses: daixp@cup.edu.cn (X. Dai), s.qiao@adelaide.edu.au (S. Qiao).

Ru- and Ni-based catalysts for CO-SMET process have been generally studied. Ni-based catalysts showed good catalytic activities, which are also affected by the nature of the support, but these catalysts were often operated either in a narrow reaction temperature range or with a lower CO concentration, which are far from practical operation conditions [15,17,18]. On the other hand, catalysts with Ru as an active component showed a high activity and selectivity toward CO methanation. Ru-based catalysts were already tested to increase the selectivity in many different ways, including the use of dopants [3,19,20] or of different support materials such as TiO_2, Al_2O_3, ZrO_2, zeolite [5,21–25]. A high Ru loading is usually required to obtain the best performance in CO-SMET. However, due to the high costs of Ru metal, the industrially used catalysts for methanation are usually based on moderately priced Ni or Fe metal supported catalysts. Disadvantage of these catalysts is the fast deactivation with time due to a higher CO disproportionation probability. Many researchers have investigated different dopants (e.g. Ru) to increase the reducibility of nickel-based catalyst [1,26], or by preparing mixed oxides (e.g. Ni-Re-Y) [4] in order to improve the catalytic performance. High Ni dispersion and modified surface, which is favoring the adsorption of H_2 and CO while disfavoring CO_2 adsorption, can play an important role in enhancing the activity and selectivity. It is reported that CO methanation over supported metal catalysts proceeds via the dissociation of CO on the metal and the successive hydrogenation of the resultant surface carbonaceous species [27]. Increase of H_2 adsorbed dissociatively on metal species is likely to enhance the CO methanation activity. TiO_2 as a kind of new-type support arouses public attention in CO-SMET [3,15,26,28–31]. The beneficial effect of TiO_2 support for CO methanation has been reported by several authors. Wang et al. [32] reported that specific activity of Pd increases by more than two orders of magnitude using TiO_2 as support, due to strong interaction between Pd crystallites and the support. Boffa et al. [33] suggested that the enhancement of CO and CO_2 hydrogenation over TiO_x is attributed to the formation of Lewis acid-base complexes between the oxygen end of adsorbed CO and anionic vacancies present at the edge of the oxide–metal boundary. However, it does not possess large specific surface area. Other researchers suggested the advantageous effect for methanation based on strong metal–support interactions by modified support. Wang et al. [34] reported that the addition of ZrO_2 promoter results in stronger acid strength and larger amounts of acid of the ZrO_2–SiO_2 support, and thus lead to an increase of the interaction between NiO species and ZrO_2–SiO_2 support and high CO methanation performance. TiO_2–Al_2O_3 mixed oxides can retain the benefits of both TiO_2 and Al_2O_3, and increase the amount of weak and strong acid centers owing to the presence of titanium cations in an electron-deficient environment [35,36]. The main role of TiO_2 appeared to be two-fold: (a) inhibition of the formation of hardly reducible spinel-like species and (b) increased dispersion of the Ni metallic phase [37]. Recently, studies have been conducted exploring the use of mesoporous materials as supports to immobilize metal/metal oxide catalysts within the mesopores, which can prevent sintering of nanoparticles by confinement [38]. The effective loading of active species into the pore network of the mesoporous supports determines their catalytic performance to a large extent. Some efforts were made by in situ incorporation of nickel or noble metal nanoparticles into aluminum oxide frameworks [1,39–44]. This led to high dispersion of active centers and spatial isolation from each other, which is of great importance to obtain higher resistance against sintering [40]. Moreover, high dispersion of metal particles over mesoporous materials seems to provide more "accessible" active sites [45], which usually show greatly enhanced catalytic activity owing to the high surface area and high density of active sites on the surface of nanoparticles [46,47].

Herein, based on a sol–gel process combined to porosity control using soft-templating according to the evaporation-induced self-assembly (EISA) method, we propose a facile one-pot approach to synthesize RuNi-doped TiO_2–Al_2O_3 nanocomposites containing trace Ru. The catalysts show evenly distributed active centers, large-pore mesopores and high surface area. The small nanoparticles are uniformly embedded within the mesoporous framework, which is highly advantageous for the retention of open pores to favor for the selective CO methanation performance in H_2-rich reformates gas. The resultant MRAT-30Ni nanocomposite shows excellent catalytic performance, with outlet CO concentration less than 50 ppm and working temperature window of close to 50 °C, which almost covers the typical working range of conventional upstream low-temperature shift reactors. Long-term stability testing for MRAT-30Ni catalyst reveals no detectable change in outlet CO and CH_4 concentrations at 200 h time on stream. The large-pore mesoporous catalysts doped with trace Ru, which are based on a facile one-pot synthesis, achieved the requirements of high purity hydrogen in PEMFC applications, starting from the high concentration of 1 vol% CO in the inlet gas and reaching levels below 20 ppm with such long-term stability.

2. Materials and methods

2.1. Catalyst preparation

Large-pore mesoporous RuNi-doping TiO_2–Al_2O_3 nanocomposites were synthesized by evaporation induced self-assembly using triblock copolymer EO_{20}-$PO_{70}EO_{20}$ (Pluronic P123) as the soft template. All reagents were analytical-grade, supplied by Sigma Aldrich, except for $Ni(NO_3)_2 \cdot 6H_2O$ (Fluka, Co.), 70% HNO_3 (Labscan, Co.), and anhydrous ethanol (Fluka, Co.), and used as received without further purification. RuNi-doped TiO_2–Al_2O_3 nanocomposites (denoted as MRNAT-xNi) were systematically prepared at various molar fractions of nickel to aluminum and titanium ($x = Ni/(Ni + Al + Ti) \times 100 = 0, 5, 10, 20, 30, 40, 50,$ mol), $Ti/(Ti + Al) \times 100 = 6.8$ (mol) with fixed amount of Ru (1 wt.%, $Ru/(Al_2O_3 + TiO_2) \times 100$). Typically, m(P123, g)/n(M^{n+}, mmol), v(HNO_3, ml)/n(M^{n+}, mmol) and were kept constant as 0.1 and 0.16, respectively. In a typical synthesis, $Ni(NO_3)_2 \cdot 6H_2O$ (0.734 g, 2.524 mmol) and $RuCl_3 \cdot xH_2O$ (0.029 g, 0.124 mmol), the Ni and Ru precursor respectively, were dissolved with the P123 triblock copolymer template (2.44 g) in anhydrous ethanol (24.4 ml) with stirring for 4 h at room temperature. Then, 4.178 g of 98% aluminum isopropoxide (20.46 mmol) and 0.184 g of TiF_4 (1.49 mmol) were dissolved in 4.04 ml of 70 wt.% HNO_3 and 12.6 ml anhydrous ethanol. Once dissolved, the two solutions were mixed quickly. This combined solution was continuously stirred at room temperature for another 20 h. Solvent evaporation was performed at 60 °C for 48 h in air. The resultant samples were calcined at 400 °C for 5 h with a heating rate of 1 °C/min in air.

For comparison of the catalytic performance, Ni/TiO_2–Al_2O_3 and Ru–Ni/TiO_2–Al_2O_3 catalysts (Al_2O_3, CONDEA Chemie GmbH), which are of the same composition as MRNAT-30Ni, were prepared by conventional impregnation method. Al_2O_3 was firstly modified with TiF_4, and calcined at 400 °C for 5 h. Then, the resulted TiO_2–Al_2O_3 support was used to prepare Ni/TiO_2–Al_2O_3 and Ru–Ni/TiO_2–Al_2O_3 catalysts by impregnation with an ethanol solution of $Ni(NO_3)_2$ and $RuCl_3$. The resultant sample was calcined at 400 °C for 5 h under air with a heating rate of 1 °C/min.

2.2. Catalyst characterization

Thermogravimetric analysis (TGA) was performed in a Gas Controller GC2000 Starsystem at high-resolution mode. The MRNAT-xNi catalysts (10–20 mg) were placed in a quartz crucible,

and were dehydrated in dry air at 400 °C for 3 h. Then the samples were cooled down to room temperature. After that treatment, the curves were recorded in flowing air (20 ml/min) with a heating rate of 10 °C/min up to 900 °C. The reduction degree of MRNAT-xNi in hydrogen was also measured by TGA. After that the same pretreatment, the catalysts were heated in 5% H_2 in N_2 from room temperature to 400 °C for 2 h with a heating rate of 5 °C/min. The data were corrected and normalized.

Infrared spectra were collected on dried samples by the attenuated total reflectance (ATR) method using a Nicolet 5700 FTIR spectrometer (Thermo Electron Corp, Madison, WI) equipped with a Nicolet Smart Orbit ATR accessory incorporating a diamond internal reflection element. Spectra were collected for all the samples at a resolution of 2 cm^{-1} in the range 4000–400 cm^{-1} for a total of 32 scans and are not corrected for penetration depth variation.

Powder X-ray diffraction (XRD) was measured with (Bruker Miniflex goniometer) using Co Kα (λ = 0.1789 nm) radiation which is calculated from the peaks of NiO (2 0 0) of by $\lambda = 2d_{hkl} \cdot \sin\theta$ (Bragg's law) and $d_{hkl} = a/(\sqrt{h^2 + k^2 + l^2})$ (for cubic crystal) [48]. Where d_{hkl} is the distance between adjacent planes in the $(h\,k\,l)$ set, a is the lattice parameter, and h, k and l are the indices of the planes.

X-ray photoelectron spectroscopy (XPS) was performed on ESCALABMkII spectrometer (VG Scientific), by unmonochromatized MgKα radiation (1253.6 eV). The total instrument resolution was 1.5 eV (measured from the Ag5d5/2 line width). The energy scale was calibrated by the Al2p line (74.5 eV). Detailed spectra are processed using CasaXPS software (V2.3.14, Casa Software Ltd., UK). An integrated Shirley-Sherwood background subtraction was applied before peak fitting, using the product of Gaussian and Lorentzian functions and applying a Marquardt least-squares algorithm. All surface atomic ratios are corrected from the high-resolution spectra using the instrumental sensitivity factor, which for Ni2p, Ti2p3/2, and Al2p peaks are 4.5, 1.2 and 0.185, respectively.

The Ru and Ni loading were determined by inductively coupled plasma optical emission spectrometry (ICP-OES) with EPA protocol 3052. The digested sample was analyzed using a Varian Vista Pro ICPOES instrument.

Nitrogen adsorption/desorption measurements were conducted on Tristar analyzer at 77 K (−196 °C) in liquid nitrogen. The Brunauer–Emmett–Teller (BET) surface area was calculated using experimental points in a relative pressure range of P/P_0 = 0.05–0.30. Pore size analysis was performed by applying nonlocal density functional theory (NLDFT) methods [49–51]. The implemented NLDFT model considering sorption of nitrogen at −196 °C in cylindrical silica pores (oxide model) was supplied by the Quantachrome Autosorb 1.55 software (Quantachrome Instruments, USA). In the mesopore range, silica can be viewed as a reasonable approximation of an oxidic surface [49–52]. Here, the kernel of (metastable) NLDFT adsorption isotherms (adsorption branch) was applied for pore width determination. Note that, the fits between experimental and theoretical isotherms were satisfactory in the capillary condensation range, which is the range relevant for the pore size analysis. The total pore volume was estimated by the nitrogen amount adsorbed at a relative pressure (P/P_0) of 0.99.

Transmission electron microscopy (TEM) images were obtained on JEM 1010. High-resolution transmission electron microscopy (HRTEM) images of MRNA-30Ni catalyst were obtained on JEOL JSM-2100 equipped with a Link-ISIS-300 energy-dispersive X-ray spectrometer (EDS) operated at an accelerating voltage of 200 kV.

2.3. Catalytic tests

The catalytic activity tests were performed with a fixed-bed quartz tubular reactor at atmospheric pressure. In a typical methanation reaction, 0.2 g of catalyst was reduced in H_2 at 400 °C for 2 h before use. When the oven was cooled down to 170 °C, the gas was switched to the feed gas which contained 1 vol% CO, 20 vol% CO_2, 50 vol% H_2 and 29 vol% He. The gas hourly space velocity (GHSV) was 2400 h^{-1}. The reaction temperatures were measured with thermocouples below the catalyst layer.

The stability tests for selective CO methanation were carried out in a fixed-bed tubular reactor at atmospheric pressure and 216 °C. 0.5 g of catalysts were placed in the reactor, and then reduced at 400 °C for 2 h in H_2 flow prior to each run. The feed gas consists of 0.8 vol% CO, 17.3 vol% CO_2, 68.3 vol% H_2 and 13.6 vol% H_2O. The gas hourly space velocity (GHSV) was adjusted to 2400 h^{-1} on a dry basis.

The gas from the reactor was analyzed by an on-line Agilent 6890 GC. CO, CO_2 and CH_4 were separated by two-tandem packed column 5A molecular sieve and Porapark Q, and detected by TCD. Traces of CO were analyzed though the separation by a molecular sieve column and methanation, then detected by FID equipped with a plot Al_2O_3 capillary column. To determine the catalytic activity, the CO and CO_2 conversion, CH_4 selectivity and CO concentration in outlet gas were calculated as follows:

$$X_{CO}(\%) = \frac{CO_{inlet} - CO_{outlet}}{CO_{inlet}} \times 100\%$$

$$X_{CO_2}(\%) = \frac{CO_{2,inlet} - CO_{2,outlet}}{CO_{2,outlet}} \times 100\%$$

$$CH_4\ selectivity(\%) = \frac{CO_{inlet} - CO_{outlet}}{(CO_{inlet} - CO_{outlet}) + (CO_{2,inlet} - CO_{2,outlet})} \times 100\%$$

$$CO\ concentration\,(ppm) = \frac{1 - X_{CO}}{100 - X_{CO} \times 3 - 20 \times X_{CO_2} \times 4} \times 10^6$$

$$H_2\ consumption(\%)$$
$$= \frac{3 \times [CO_{inlet} - CO_{outlet}] + 4 \times [CO_{2,inlet} - CO_{2,outlet}]}{H_{2,inlet}} \times 100$$

where $X_{CO} \times 3$ and $20 \times X_{CO_2} \times 4$ are the reduction in volume after methanation of CO and CO_2 excluded the effect of steam, respectively. $H_{2,inlet}$ is defined as the amount of H_2 in reformate gas.

3. Results and discussion

3.1. Characterization of As-prepared MRNAT-xNi materials

3.1.1. Powder XRD analysis

A series of large-pore mesoporous NiRu-doping TiO_2–Al_2O_3 nanocomposites were synthesized by the facile one-pot method using the EISA procedure [46] as shown in Scheme 1. Convincing evidence for the effective template removal from the as-prepared samples has been confirmed by TGA and FT-IR spectra (Figs. S1 and S2). The wide-angle X-ray diffraction (WXRD) patterns of the different powders indicate a low level of crystallinity for MRNAT-xNi calcined at 400 °C (Fig. 1A). Interestingly, no peaks for individual NiO, RuO_2 and TiO_2 are observed for the MRNAT-xNi samples with x < 30. This seems to suggest that NiO and TiO_2 remain highly dispersed in the mesoporous alumina matrix, and form homogeneous mixtures [53]. When x = 30, broad peaks assigned to NiO are observed, which become more intense at higher Ni fractions. The diffraction peaks at 2θ positions of 43.5°, 50.7° and 74.6° can be indexed to the (1 1 1), (2 0 0) and (2 2 0) planes of cubic-phased NiO (JCPDS card No. 47-1049). The main diffraction peak at 2θ = 50.7°
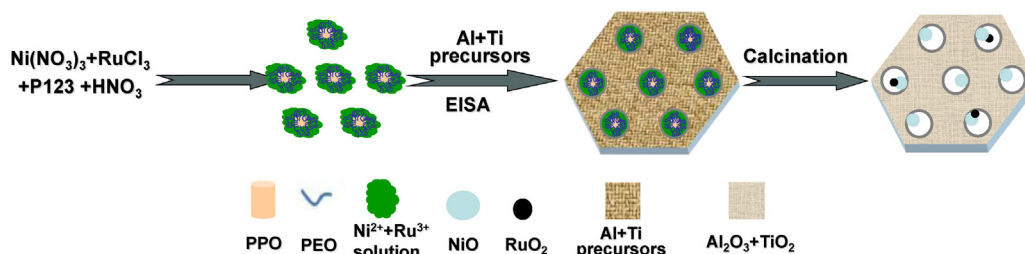
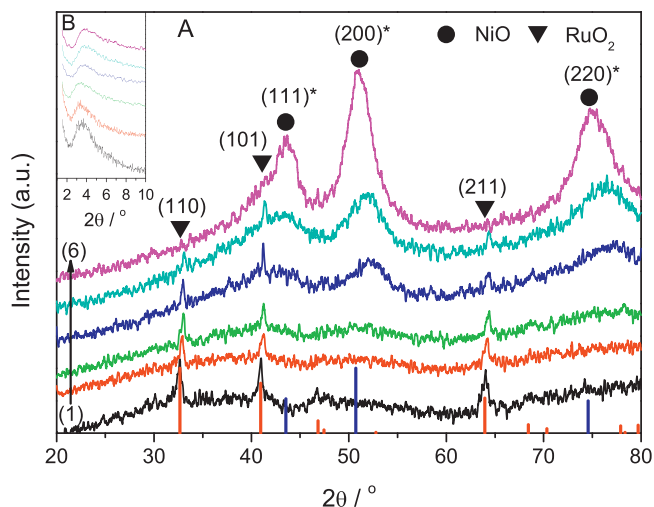**Scheme 1.** Schematic representation of the preparation of the MRNAT-xNi composite catalysts.

Fig. 1. Wide-angle (A) and small-angle (B) XRD patterns of fresh MRNAT-xNi samples (from (1)–(6), with x = 0, 5, 10, 20, 30 and 40, respectively). The diffraction peaks are indexed for RuO$_2$ [(h k l), JCPDS card No. 43-1027, (red sticks)] and NiO [(h k l)*, JCPDS card No. 47-1049 (blue sticks)]. (For interpretation of the references to color in text/this figure legend, the reader is referred to the web version of the article.)

shifts to lower angles with increasing amount of NiO, implying the increasing lattice parameter of the nanocomposites. The variation of the lattice parameter with increasing NiO fraction is shown in Table 1. We can see that the lattice parameter of NiO decreases from 4.170 to 4.072 nm with increasing Ni content. The representative small-angle powder XRD patterns show a single broad peak (Fig. 2B), which is characteristic of mesoporous structure with limited long-range order in terms of the pore arrangement (i.e., the pores are not very well-ordered in these materials), similarly to the mesoporous alumina obtained by hydrothermal synthesis or microwave methods [54]. Three peaks at 2θ positions of 32.7°, 40.9° and 63.9° are observed on MRNAT-xNi samples (x = 0, 5, 10, 20 and 30), which are attributed to the tetragonal RuO$_2$ (1 1 0), (1 0 1) and (2 1 1) facets, respectively, confirming the presence of RuO$_2$ particles. Compared to those of the reference file (JCPDS card No. 43-1027), the diffraction peaks shift slightly toward higher 2θ

values with increased Ni content, indicative of the smaller lattice parameters of RuO$_2$ compared to those of the reference compound.

By measuring the full width at half-maximum (FWHM) of the strongest diffraction peak at 50.7°, the average crystallite size of NiO was estimated according to the Scherrer equation. The MRNAT-30Ni sample shows a larger NiO average crystallite size (13.1 nm) than that in MRNAT-20Ni (10.3 nm) and MRNAT-40Ni (6.5 nm) samples (see Table 1). Since the crystallographic structure of RuO$_2$ is tetragonal, the value of the lattice parameters a and c can be calculated directly from the position of the (1 1 0) and (2 1 1) diffraction peaks, respectively [55]. The lattice parameter a has a tendency to decrease with higher nickel fraction, while the lattice parameter c remains remarkably constant. On the other hand, the FWHM of RuO$_2$ (1 1 0) peak decreases with the increasing nickel fraction. It is well known that the XRD peak becomes shaper when the grain size increases or the crystallinity improves [25]. Compared with traditional impregnation methods, the addition of the amphiphilic block copolymer (P123) seems favorable for a higher crystallization degree and improved distribution of RuO$_2$ particles (Supporting Information, Fig. S3a and c). The XRD spectra of post-reaction MRNAT-30Ni sample for 200 h time on stream displays two weak and broad diffraction peaks at 2θ value of ~44° and ~51.8°, which is characteristic of small Ni crystallites, while two strong diffraction peaks are observed on post-reaction Ru–Ni/TiO$_2$–Al$_2$O$_3$ samples for 200 h time on stream (Supporting Information, Fig. S3b and d). The results suggest that Ni insertion into the alumina matrix by one-pot strategy has effectively prevented the aggregation of the Ni metal particles by confinement effect.

3.1.2. Nitrogen adsorption/desorption measurements

The pore structure of all of the samples with varied Ni content were examined by N$_2$ adsorption/desorption isotherms, as shown in Fig. 2. All samples exhibit an obvious type IV isotherm with H1 hysteresis loop characteristic of large cylindrical mesopores. The steep capillary condensation step at P/P_0 = 0.75–0.90 clearly reflects large mesopores [56]. As can be seen from Fig. 2A, the steepness of the capillary condensation step is maintained with increasing molar fraction of Ni to MRNAT-20Ni. This condensation step slightly shifts to higher relative pressures as the pore size increase. The NLDFT pore size distributions deduced from adsorption branch of samples MRNAT-xNi with x = 0–20 show a

Table 1
Lattice parameter a and particle size of NiO and RuO$_2$ with different Ni fractions.

Sample	NiO lattice parameter a (Å)			NiO particle size (nm)[a]	NiO particle size (nm)[b]	RuO$_2$ lattice parameter a, c (Å)			
	2θ (2 0 0) (°)	d$_{200}$	a			2θ (1 1 0) (°)	a	2θ (2 1 1) (°)	c
MRNAT-0Ni	–	–	–	–	–	32.66	4.501	64.04	3.097
MRNAT-5Ni	–	–	–	–	–	32.92	4.467	64.36	3.115
MRNAT-10Ni	–	–	–	–	–	32.99	4.458	64.44	3.111
MRNAT-20Ni	52.16	2.036	4.072	10.3	8.1	33.02	4.454	64.47	3.113
MRNAT-30Ni	51.80	2.049	4.098	13.1	9.2	33.10	4.443	64.45	3.114
MRNAT-40Ni	51.06	2.084	4.170	6.5	6.7	–	–	–	–

[a] XRD.
[b] TEM.

Table 2
Physicochemical parameters of MRNAT-xNi composites calcined at 400 °C for 5 h, derived from N_2 sorption at 77 K, NiO reduction degree and activation energy of CO-SMET.

Sample	S_{BET} (m^2/g)[a]	Total pore V_{sp} (cm^3/g)[b]	Pore diameter (nm)[c]	NiO reduction degree (%)	CO$_2$ conversion[e] E_a (kJ/mol)	CO conversion[e] E_a (kJ/mol)
MRNAT-0Ni	239	1.08	13.9 (19.5)[d]	–	–	–
MRNAT-5Ni	206	0.97	13.9 (25.5)[d]	66.0	111.9	80.9
MRNAT-10Ni	209	0.99	13.9 (23.5)[d]	41.6	94.3	89.8
MRNAT-20Ni	187	0.94	16.1 (24.5)[d]	29.0	101.3	85.10
MRNAT-30Ni	218	0.79	6.1, 15.5	51.4	81.6	104.9
MRNAT-40Ni	221	0.58	5.85, 13.0	56.6	74.3	84.3
Ni/MgAl$_2$O$_4$ [57]	–	–	–	–	–	96.7[f]
FeNi/MgAl$_2$O$_4$ [58]	–	–	–	–	–	90–11[g]
Ni/SiO$_2$ [59]	–	–	–	–	96[h]	80[h]
RuNi/SiO$_2$ [60]	–	–	–	–	81.9[i]	–
Ru/Al$_2$O$_3$ [19]	–	–	–	–	76.9[j]	–

[a] Surface area determined from adsorption data in the P/P_0 = 0.05 to 0.3 using the BET equation.
[b] Total pore volume obtained from the adsorption isotherm at P/P_0 = 0.99.
[c] Pore size determined at the maximum of NLDFT pore size distribution (adsorption branch).
[d] Center value of a broad distribution associated to a minor secondary population of mesopores.
[e] Reaction condition: 1 vol% CO, 20 vol% CO$_2$, 50 vol% H$_2$ in He from 170 to 290 °C (this work).
[f] Reaction condition: 2.05 vol% CO, 97.95 vol% H$_2$ from 225 to 287 °C.
[g] Reaction condition: 2 vol% CO, 98 vol% H$_2$ from 200 to 280 °C.
[h] Reaction condition: 1 vol% CO$_2$, 4 vol% H$_2$ in N$_2$ from 223 to 327 °C.
[i] Reaction condition: 6 vol% CO$_2$, 18 vol% H$_2$ in N$_2$ from 180 to 290 °C.
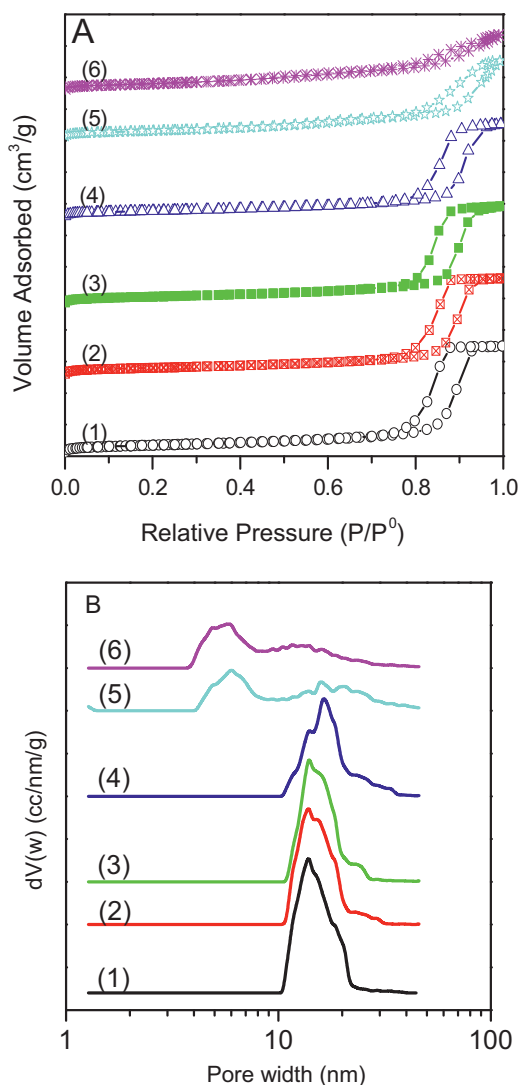[j] Reaction condition: 1 vol% CO, 15 vol% CO$_2$, 50 vol% H$_2$ in He from 200 to 300 °C.

Fig. 2. Nitrogen adsorption–desorption isotherms (N$_2$, 77 K) and NLDFT pore-size distribution curves (adsorption branch) of the fresh MRNAT-xNi composites.

first pronounced maximum centered at 14–16 nm, accompanied with a second broader distribution within the range of 20–26 nm. The pore size distributions for MRNAT-30Ni and MRNAT-40Ni are distinctively bimodal, with small pores in the range of 6 and 5.8 nm, and a second more important population at 16 and 13 nm, respectively. In the latter cases, it may suggest that the materials could present some pore windows or pore interconnections smaller than the main mesopores [57] (Fig. 2B). All the samples show high-specific surface areas up to 239 m^2/g and large pore volumes up to 1.08 cm^3/g (see Table 2). Incorporating Ni into the mesostructure results in slightly decrease of the specific surface area and pore volume values. However, an increase in the BET surface area is observed for MRNAT-30Ni and MRNAT-40Ni samples, which can be attributed to double mesoporous structure.

3.1.3. Transmission electron microscopy (TEM)

The mesopore structure of the MRNAT-xNi samples is studied by TEM (Figs. 3 and 4). Some periodicity is confirmed for the MRNAT-0Ni, MRNAT-5Ni and MRNAT-10Ni samples. The order deteriorates at high Ni loading, as illustrated in Fig. 3D–F. The grain size and morphologies of MRNAT-30Ni are also examined by HRTEM (Fig. 4A). The lattice fringes of the representative particles are 0.21, 0.24, 0.26 and 0.32 nm, which belong to the spacing of NiO(200), NiO(1 1 1), RuO$_2$(1 0 1) and (1 1 0), respectively [25]. The NiO particles have a small size ($\sim$5 nm), which is consistent with the XRD data. The particles exhibit lattice fringes for NiO(2 0 0) and RuO$_2$(1 0 1) in a same area, confirming junctions between some NiO particles and RuO$_2$ particles to form contacting RuNi particles (see the white circle in Fig. 4A). The selected area electron diffraction (SAED) pattern (inset image in Fig. 4A) shows a continuous ring type image indicative of the polycrystalline structure of NiO and RuO$_2$ in the nanocomposite, from which the Ni(2 0 0), Ni(1 1 1), Ru(1 0 1) and Ru(1 1 0) planes are indexed, respectively. In addition, elemental mapping and the compositional linear scan profiles obtained by scanning TEM-energy dispersive X-ray spectroscopy (EDS) on the MRNAT-30Ni sample (Fig. 5), show the expected metal element signals, confirming the high dispersion of Ni, Ru and Ti throughout the entire nanocomposite. Accordingly, the EDS patterns show uniform distribution of the elements (i.e. Ni, Ru, Ti and Al) in different locations. The concentrations of Ru are also obtained by elemental mapping and ICP (Supporting Information, Figs. S4–S6), and
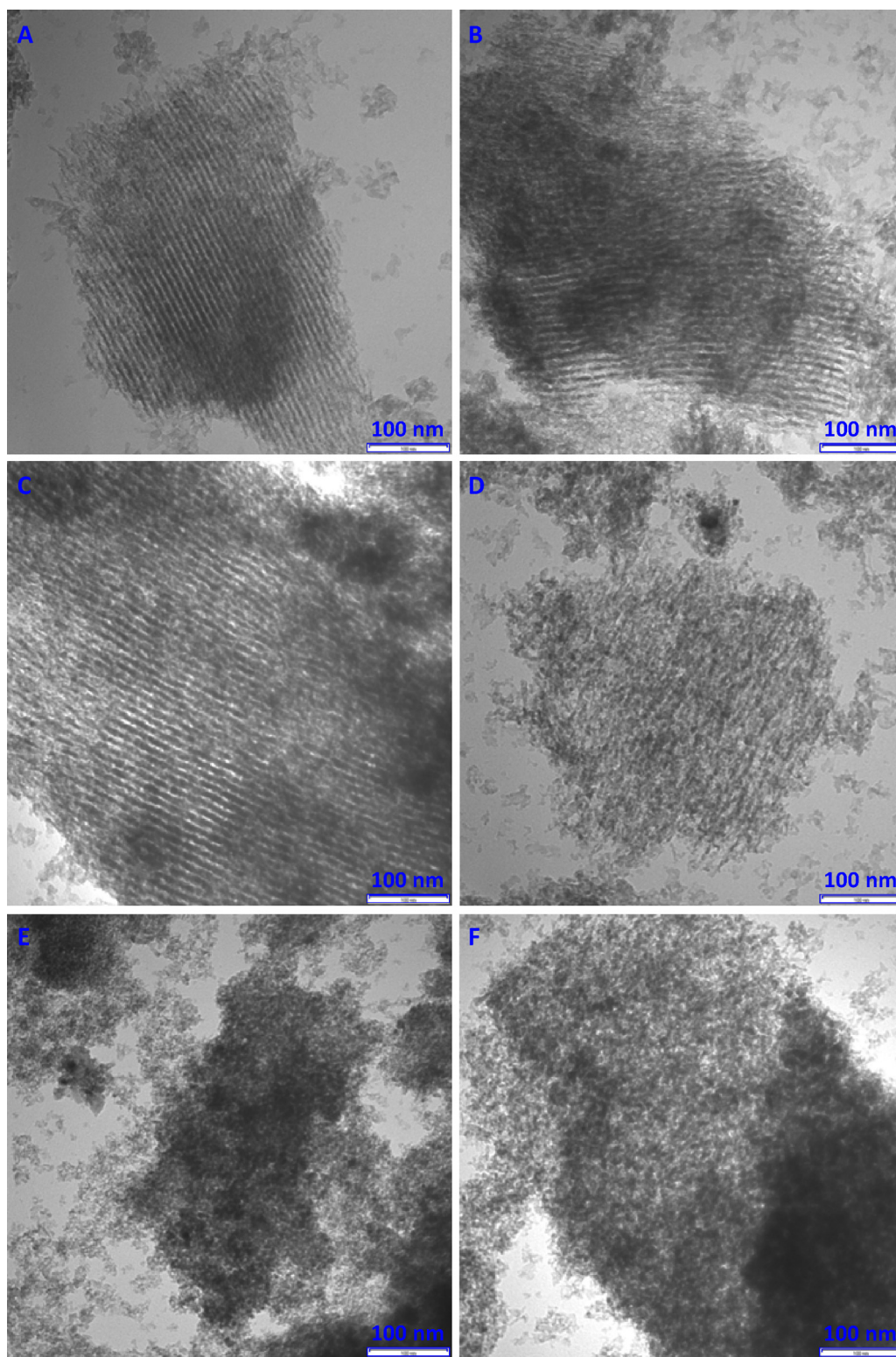
Fig. 3. TEM of the fresh MRNAT-*x*Ni samples (*x* = 0, 5, 10, 20, 30 and 40).

the uniform distribution of Ni, Ru, Ti and Al in the MRNAT-*x*Ni catalysts are also evidenced by ICP-AES and XPS analyses (Supporting Information Fig. S7 and Table S1). The results exhibit a similar surface and bulk composition in the nanocomposites, which shows no enrichment of elements. The TEM spectra of post-reaction MRNAT-30Ni sample and Ru–Ni/TiO$_2$–Al$_2$O$_3$ catalyst for 200 h time on stream indicate that the RuNi insertion into the alumina matrix by one-pot strategy has effectively prevented the aggregation of the RuNi metal particles, while the aggregation happens over the sample prepared by conventional impregnation method (in Fig. 4C and D), which also agrees with XRD characterization in Fig. S3 (Supporting Information).
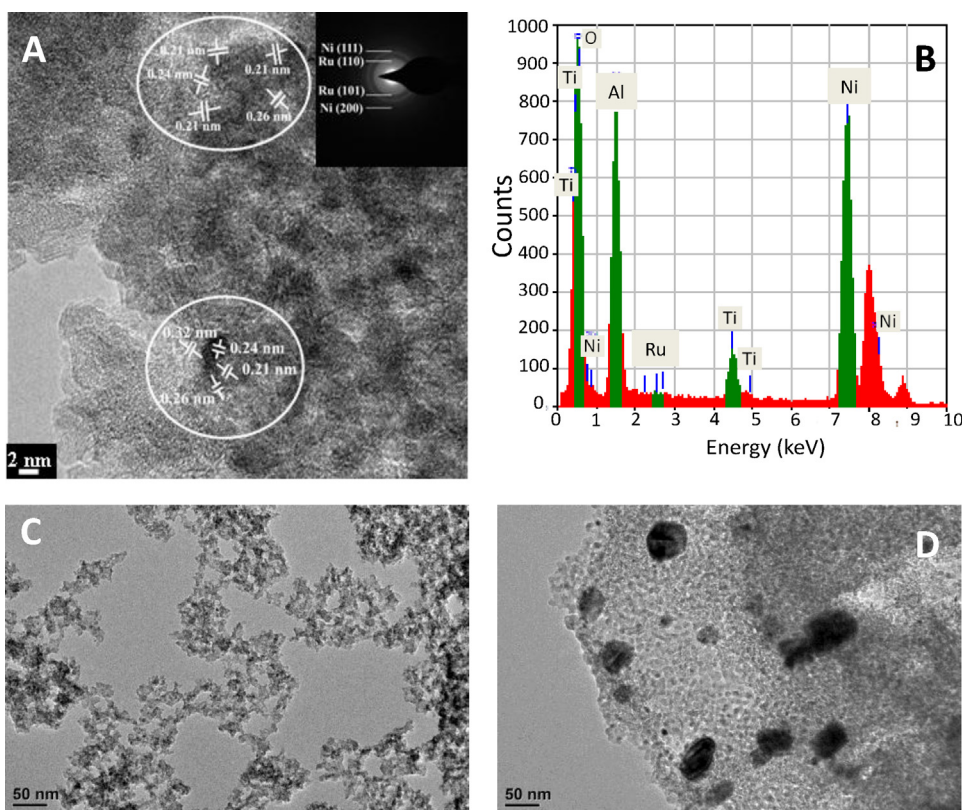
Fig. 4. HR-TEM image (A) with corresponding EDS (B) of fresh MRNAT-30Ni sample, post-reaction MRNAT-30Ni sample for 200 h time on stream (C), and post-reaction Ru–Ni/TiO₂–Al₂O₃ catalyst (D) for 200 h time on stream.

3.2. Catalytic performance of the selective CO methanation over MRNAT-xNi catalysts

3.2.1. The temperature dependence of selective CO methanation

The temperature dependence of CO and CO_2 conversions, as well as outlet CH_4 and CO concentrations, over the MRNAT-xNi catalysts is shown in Fig. 6. For all temperatures studied, an increase of the total metal content leads to a considerable increase of the methanation activity due to high active site density (Fig. 6A and B). For all the MRNAT-xNi catalysts examined, the outlet CO concentrations decrease with increasing reaction temperature, and exhibit a minimum except for MRNAT-0Ni (Fig. 6C). It is obvious that the temperature for optimal CO removal is lowered with increasing Ni content. The outlet CO concentration is below 50 ppm for MRNAT-30Ni and MRNAT-40Ni samples, and in particular, lowers than 10 ppm in the case of MRNAT-30Ni at 210 °C in Fig. 6C. At higher Ni concentrations, the outlet CO concentration increases significantly, most probably due to the blocking of internal surface of the catalyst, which was confirmed by a significant decrease of pore volume and pore diameter over MRNAT-40Ni sample (see Table 2). After reaching the minima (~14 ppm), the outlet CO concentration increases at higher temperature because of the RWGS reaction, which is thermodynamically and kinetically favored at high temperatures. It means that the reaction rate of CO methanation is lower than that of the RWGS reaction. It is also observed that the conversion of CO_2 increases at higher temperature (Fig. 6A). Because the methanation of CO_2 will consume four moles of hydrogen, and produce a large amount of reaction heat, the reaction temperature should be controlled to be as low as possible. However, it is difficult to compare the catalytic performances for CO methanation, because the CO/CO_2 conversion and selectivity, and reaction temperature are all important parameters for PEMFC applications. A set of three distinct temperatures was used to describe the

catalytic performances for Pt-alloy electrodes in PEMFC applications, comprehensively. $T^*_{99.5}$ is defined as a temperature range $(T_1–T_2)$ for CO conversion higher than 99.5%, which means that the outlet CO concentration is lower than 50 ppm in this temperature range. T_3, the value at which 5 mol% of CO_2 is converted, can be as used as a benchmark value to identify the temperature window. The difference between either T_2 or T_3 (whichever was lower) and T_1 is used to identify the temperature range for the highly selective CO conversion, and is considered as the working temperature window, which should be as large as possible. For the MRNAT-30Ni catalyst, outlet CH_4 concentration is suppressed to less than 2.0 vol%, indicating the selectivity of CO methanation is greater than 50%. The working temperature window for CO-SMET, is close to 50 °C, which nearly covers the typical working range of conventional upstream low-temperature shift reactors [58]. It also exhibits higher activity in comparison to Ni/TiO₂–Al₂O₃ and Ru–Ni/TiO₂–Al₂O₃ catalysts, which are prepared by conventional impregnation methods, with similar compositions as the MRNAT-30Ni nanocomposite (Supporting Information, Fig. S8). Yao et al. [25] prepared NiRu/SiO₂ catalyst for CO methanation using polyethylene glycol (PEG), where the close contacts between the NiO and RuO₂ particles and the uniform distribution of the RuO₂ particles has appeared to improve the promotional efficiency of Ru, because the interaction between the PEG's electron-donating groups (C–O) and cations (Ni^{2+}, Ru^{3+}) in the solvent allows the cations to maintain their well-dispersed and well-mixed status from a liquid to the surface of SiO₂ after calcination in air. A stronger synergic effect between the metals improved CO methanation performance and long-term stability (80 h) compared with conventional impregnation method. Tada et al. [26] also observed a synergic effect of Ru and Ni on TiO₂, which can enhance CO methanation and suppressed CO_2 methanation over such Ru–Ni bimetallic catalysts by decreasing in direct contact between Ru and TiO₂. In this work, the excellent performance of the MRNAT-30Ni
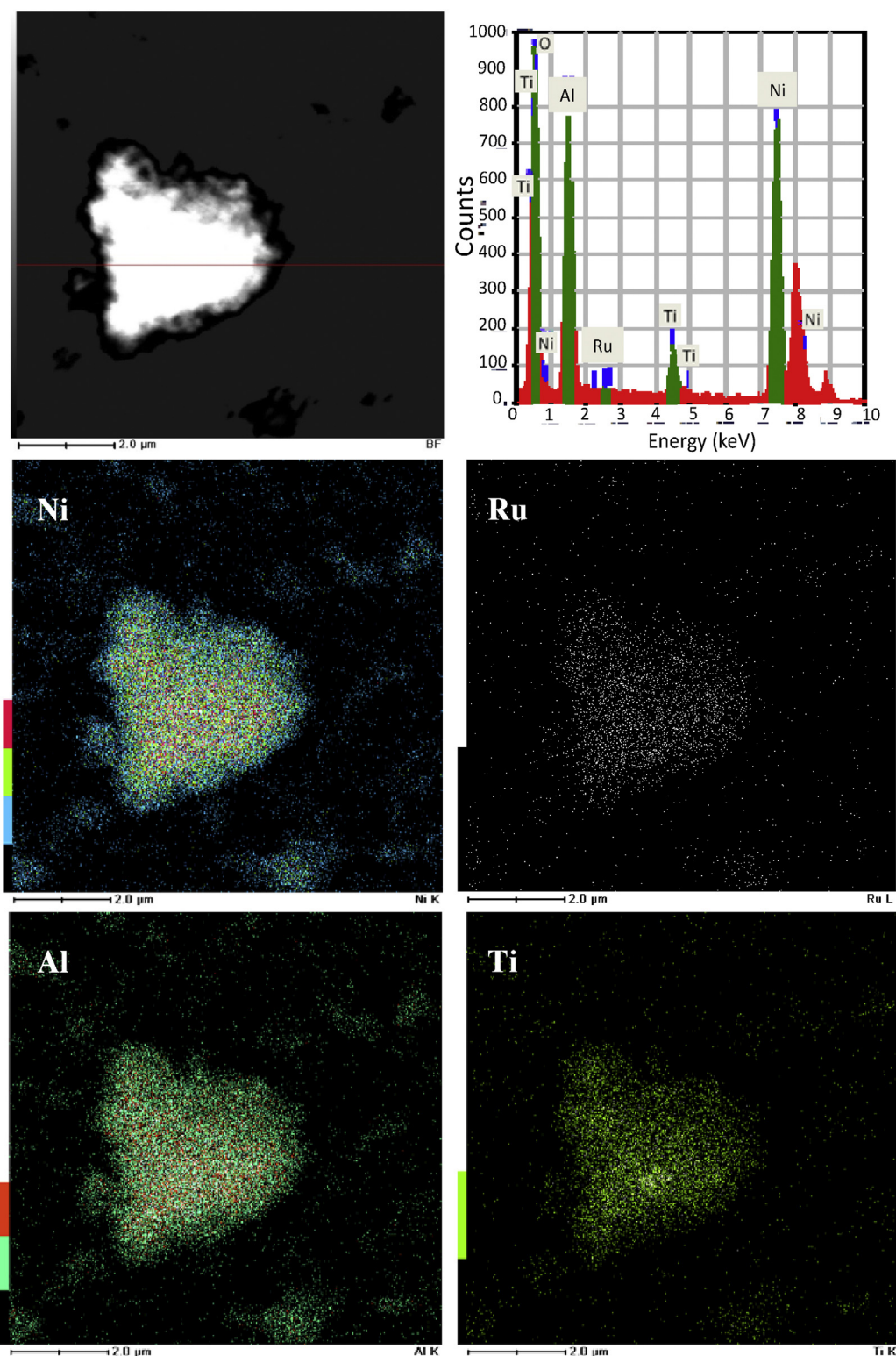
Fig. 5. TEM with corresponding EDS mapping and line scanning profiles of the fresh MRNAT-30Ni sample.

catalyst benefits from the strong interactions between the RuNi and the support with a large-pore structure and accessible active sites. It is generally known that, when a small amount of precious metal is added to a metal oxide, dissociation of hydrogen can easily take place on the precious metal sites, and increase the reduction degree of NiO owing to spill-over hydrogen from reduced Ru^0 metal sites [2,59] to form high density of active sites (Table 2), which enhance

the catalytic performance dramatically (Supporting Information, Fig. S8).

3.2.2. Long-term stability test of the MRNAT-30Ni catalyst

The long-term durability under realistic reaction conditions is another crucial factor determining the performance of a catalyst. The durability test of MRNAT-30Ni was carried out at 216 °C. Fig. 7
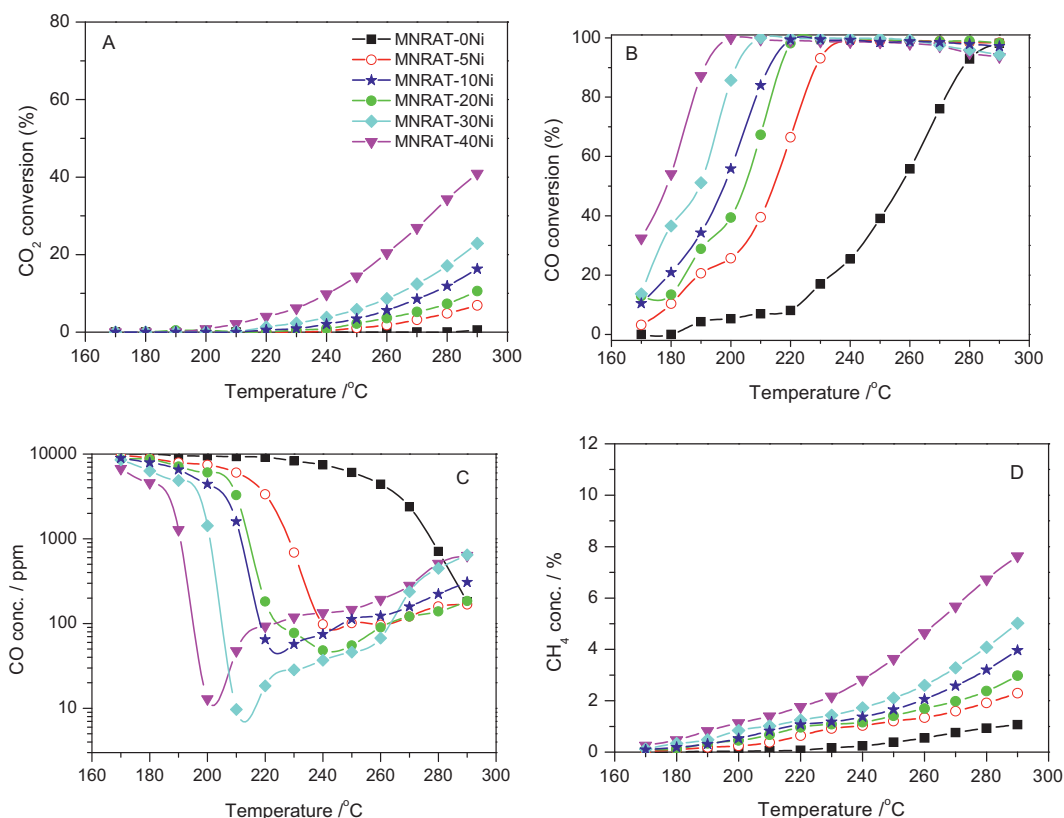
Fig. 6. Temperature dependence of (A) CO_2 and (B) CO conversion and (C) CO, (D) CH_4 outlet concentration over the MRNAT-xNi catalysts at different temperatures. Reaction conditions: 180–290 °C, 2400 h^{-1}, on a dry basis, Feed gas: 1 vol% CO, 20 vol% CO_2, 50 vol% H_2 and 29 vol% He.

shows the changes in the outlet CO, CH_4 concentrations and CH_4 selectivity as a function of time on stream. It is clear that outlet CO concentration was kept stable at less than 20 ppm over 200 h with a nearly constant CH_4 concentration of 1.4 vol% and CH_4 selectivity of 75%. This means that less than 2.0 vol. % CO_2 is simultaneously converted into methane. The total consumption of H_2 for methanation is below 6 vol%, which is very comparable to the results of CO preferential oxidation in hydrogen [5,8,60]. Thus, it was confirmed that the MRNAT-30Ni catalyst has sufficient activity and high stability in a CO removal reactor for a PEMFC system. In order to demonstrate the high stability of the MRNAT-30Ni nanocomposite, we also investigated the stability of the Ru–Ni/TiO$_2$–Al$_2$O$_3$

catalyst, which is prepared by co-impregnation method, with the same composition as the MRNAT-30Ni nanocomposite (Fig. 8). In this case, the result indicates that, the CO conversion is only about 85%. The Ru–Ni/TiO$_2$–Al$_2$O$_3$ catalyst lost almost 15% of its CO conversion over 200 h under the same experimental conditions, confirming a superior stability of the active sites in the MRNAT-30Ni as compared to the reference Ru–Ni/TiO$_2$–Al$_2$O$_3$ catalyst. Taking into account the similar composition in this study, the observed enhancement in activity and durability of the MRNAT-30Ni system can be attributed to their advantageous mesoporous structure and high dispersion of accessible active sites, effectively preventing catalyst degradation caused by migrating and sintering of the nanoparticles, which also are confirmed by TEM in Fig. 4C
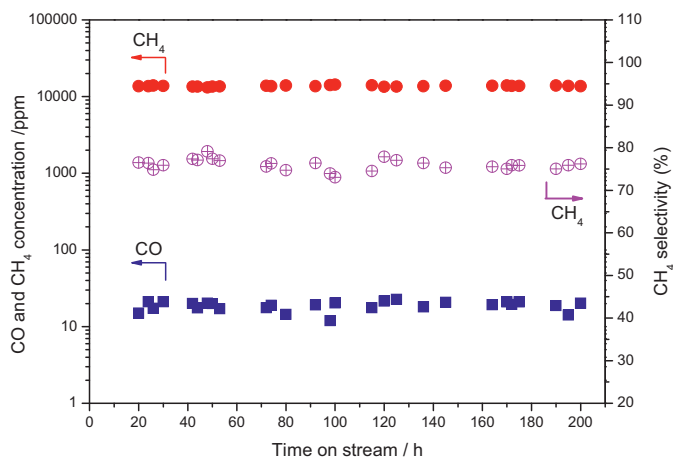

Fig. 7. Outlet CO, CH_4 concentration and CH_4 selectivity for long-term stability test over the MRNAT-30Ni catalyst. Reaction conditions: 216 °C, 2400 h^{-1} on a dry basis, Feed gas: 0.8 vol% CO, 17.3 vol% CO_2, 68.3 vol% H_2 and 13.6 vol% H_2O.
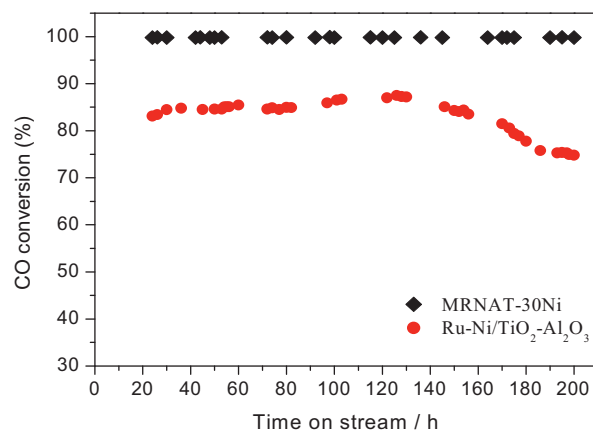

Fig. 8. Comparison of CO conversion for long-term stability test over the MRNAT-30Ni and Ru–Ni/TiO$_2$–Al$_2$O$_3$ catalysts. Reaction conditions: 216 °C, 2400 h^{-1} on a dry basis, Feed gas: 0.8 vol% CO, 17.3 vol% CO_2, 68.3 vol% H_2 and 13.6 vol% H_2O.
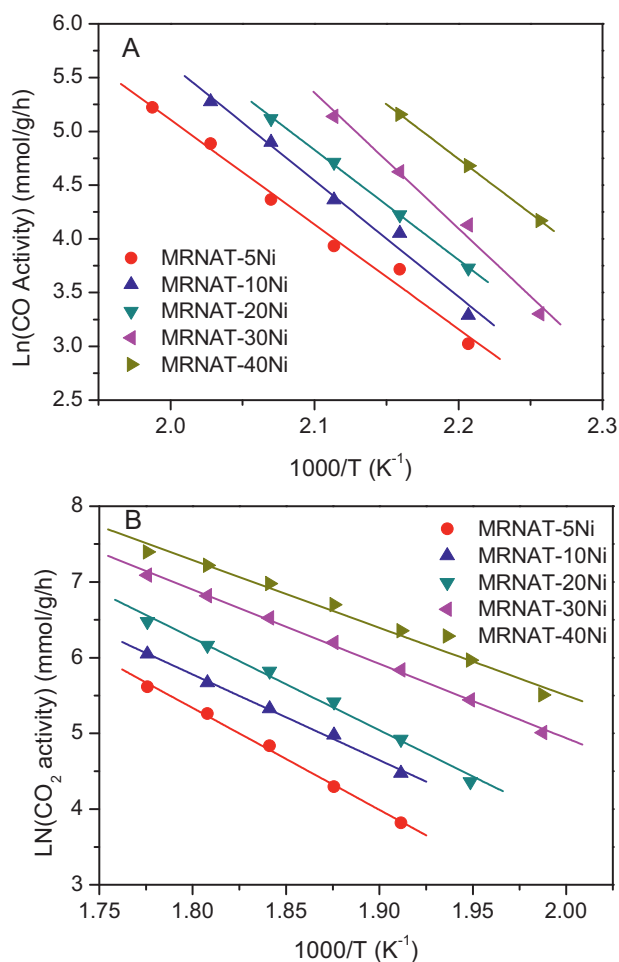
Fig. 9. Logarithm of the CO and CO_2 methanation activity as a function of 1000/T. Reaction conditions: 180–290 °C, 2400 h^{-1} on a dry basis, feed gas: 1 vol% CO, 20 vol% CO_2, 50 vol% H_2 and 29 vol% He.

and D. The results of this work suggest that it is possible to increase substantially the efficiency and stability of Ni-based methanation catalyst by doping with trace Ru based on a facile one-pot synthesis protocol.

3.2.3. Activation energies and Arrhenius plots

It is of interest to determine the temperature dependence of the rate constant for the CO and CO_2 methanation. Arrhenius plots for the catalyst were presented in Fig. 9, and the apparent activation energy (E_a) of the CO and CO_2 methanation in H_2-rich reformate gas over MRNAT-xNi catalysts were calculated from the slopes of the best-fit line in Fig. 9. The results are summarized in Table 2. It is observed that activation energies for CO and CO_2 methanation depend, to a large extent, on the nickel loading, changing in the range of 80–104.2 kJ/mol and 74.3–111.8 kJ/mol, respectively. Kimura et al. [2] proposed that the methanation of CO took place predominantly over highly dispersed Ni metal sites formed by the reduction of the Ni–Al oxides. The activation energy for CO and CO_2 methanation over MRNAT-xNi determined here is in good agreement with those reported for supported nickel catalysts or ruthenium catalysts under similar reaction conditions [61–63].

4. Conclusion

In this contribution, we have reported a facile one-pot synthesis protocol to prepare highly dispersed NiO particles on TiO_2–Al_2O_3 nanocomposites with trace Ru. The nanocomposites show large-pore mesoporous structures, high surface area, uniform pore size and homogeneous framework compositions. The high density of active sites, the open architecture and beneficial synergetic effects make the MRNAT-30Ni an excellent catalyst for CO-SMET. The working temperature window over the MRNAT-30Ni catalyst, in which CO is removed to less than 50 ppm from 1 vol.% with selectivity greater than 50.0% for the CO methanation, is close to 50 °C and almost covering the typical working range of conventional upstream low-temperature shift reactors. Furthermore, long-term stability (200 h) for CO-SMET over MRNAT-30Ni is confirmed under realistic reaction conditions, with no detectable change in the outlet CO and CH_4 concentrations. These features clearly demonstrated the advantages of the facile one-pot synthesis process, which produces catalysts with high activity and stability, being promising candidates for use in fuel processing applications.

Acknowledgements

Appendix A. Supplementary data

Supplementary data associated with this article can be found, in the online version, at http://dx.doi.org/10.1016/j.apcatb.2014.10.069.

References

[1] A.H. Chen, M. Toshihiro, H. Kazutoshi, Y. Hisao, W. Masahiro, Angew. Chem. Int. Ed. 49 (2010) 9895–9898.
[2] M. Kimura, T. Miyao, S. Komori, A. Chen, K. Higashiyama, H. Yamashita, M. Watanabe, Appl. Catal. A: Gen. 379 (2010) 182–187.
[3] P. Panagiotopoulou, D.I. Kondarides, X.E. Verykios, J. Phys. Chem. C 115 (2011) 1220–1230.
[4] M. Krämer, M. Duisberg, K. Stöwe, W.F. Maier, J. Catal. 251 (2007) 410–422.
[5] D. Gamarra, C. Belver, M. Fernández-García, A. Martínez-Arias, J. Am. Chem. Soc. 129 (2007) 12064–12065.
[6] P. Lakshmanan, J.E. Park, E.D. Park, Catal. Surv. Asia 18 (2014) 75–88.
[7] K. Liu, A.Q. Wang, T. Zhang, ACS Catal. 2 (2012) 1165–1178.
[8] S. Alayoglu, A.U. Nilekar, M. Mavrikakis, B. Eichhorn, Nat. Mater. 7 (2008) 333–338.
[9] B.T. Qiao, A.Q. Wang, X.F. Yang, L.F. Allard, Z. Jiang, Y.T. Cui, J.Y. Liu, J. Li, T. Zhang, Nat. Chem. 3 (2011) 634–641.
[10] H. Yen, Y. Seo, S. Kaliaguine, F. Kleitz, Angew. Chem. Int. Ed. 51 (2012) 12032–12035.
[11] T. Shodiya, O. Schmidt, W. Peng, N. Hotz, J. Catal. 300 (2013) 63–69.
[12] Q. Fu, W.X. Li, Y.X. Yao, H.Y. Liu, H.Y. Su, D. Ma, X.K. Gu, L.M. Chen, Z. Wang, H. Zhang, B. Wang, X.H. Bao, Science 328 (2010) 1141–1144.
[13] B.A. Wilhite, M.A. Schmidt, K.F. Jensen, Ind. Eng. Chem. Res. 43 (2004) 7083–7091.
[14] P. Panagiotopoulou, D.I. Kondarides, X.E. Verykios, Ind. Eng. Chem. Res. 50 (2011) 523–530.
[15] K. Urasaki, Y. Tanpo, Y. Nagashima, R. Kikuchi, S. Satokawa, Appl. Catal. A: Gen. 452 (2013) 174–178.
[16] E.D. Park, D. Lee, H.C. Lee, Catal. Today 139 (2009) 280–290.
[17] S. Takenaka, T. Shimizu, K. Otsuka, Int. J. Hydrogen Energy 29 (2004) 1065–1073.
[18] M.M. Zyryanova, P.V. Snytnikov, Y.I. Amosov, S.A. Ven'yaminov, E.Z. Golosman, V.A. Sobyanin, Kinet. Catal. 51 (2010) 907–913.
[19] M. Krämer, K. Stöwe, M. Duisberg, F. Müller, M. Reiser, S. Sticher, W.F. Maier, Appl. Catal. A: Gen. 369 (2009) 42–52.
[20] M.B.I. Choudhury, S. Ahmed, M.A. Shalabi, T. Inui, Appl. Catal. A: Gen. 314 (2006) 47–53.
[21] P. Djinović, C. Galletti, S. Specchia, V. Specchia, Catal. Today 164 (2011) 282–287.
[22] P. Panagiotopoulou, D.I. Kondarides, X.E. Verykios, Appl. Catal. B: Environ. 88 (2009) 470–478.
[23] C. Galletti, S. Specchia, V. Specchia, Chem. Eng. J. 167 (2011) 616–621.
[24] Y.H. Kim, E.D. Park, H.C. Lee, D. Lee, Appl. Catal. A: Gen. 366 (2009) 363–369.

[25] N. Yao, H.F. Ma, Y. Shao, C.K. Yuan, D.Y. Lv, X.N. Li, J. Mater. Chem. 21 (2011) 17403–17412.
[26] S. Tada, R. Kikuchi, A. Takagaki, T. Sugawara, S.T. Oyama, K. Urasaki, S. Satokawa, Appl. Catal. B: Environ. 140–141 (2013) 258–264.
[27] J. Kopyscinski, T.J. Schildhauer, F. Vogel, S.M.A. Biollaz, A. Wokaun, J. Catal. 271 (2010) 262–279.
[28] S. Tada, R. Kikuchi, A. Takagaki, T. Sugawara, S.T. Oyama, S. Satokawa, Catal. Today 232 (2014) 16–21.
[29] S. Tada, D. Minori, F. Otsuka, R. Kikuchi, K. Osada, K. Akiyama, Fuel 129 (2014) 219–224.
[30] S. Tada, R. Kikuchi, K. Wada, K. Osada, K. Akiyama, S. Satokawa, Y. Kawashima, J. Power Sources 264 (2014) 59–66.
[31] P. Panagiotopoulou, D.I. Kondarides, X.E. Verykios, Catal. Today 181 (2012) 138–147.
[32] S.Y. Wang, S.H. Moon, M. Albert Vannice, J. Catal. 71 (1981) 167.
[33] A. Boffa, C. Lin, A.T. Bell, G.A. Somorjai, J. Catal. 149 (1994) 149–158.
[34] Y.Z. Wang, R.F. Wu, Y.X. Zhao, Catal. Today 158 (2010) 470–474.
[35] G.S. Walker, E. Williams, A.K. Bhattacharya, J. Mater. Sci. 32 (1997) 5583–5592.
[36] M. Yang, Y. Men, S.L. Li, G.W. Chen, Appl. Catal. A: Gen. 433–434 (2012) 26–34.
[37] J. Escobar, J.A. De Los Reyes, T. Viveros, Appl. Catal. A: Gen. 253 (2003) 151–163.
[38] H. Tan, K. Li, S. Sioud, D. Cha, M.H. Amad, M.N. Hedhili, Z.A. Al-Talla, Catal. Commun. 26 (2012) 248–252.
[39] Z.X. Li, F.B. Shi, L.L. Li, T. Zhang, C.H. Yan, Phys. Chem. Chem. Phys. 13 (2011) 2488–2491.
[40] W.Q. Cai, J.G. Yu, C. Anand, A. Vinu, M. Jaroniec, Chem. Mater. 23 (2011) 1147–1157.
[41] S.M. Morris, P.F. Fulvio, M. Jaroniec, J. Am. Chem. Soc. 130 (2008) 15210–15216.
[42] L.L. Xu, H.L. Song, L.J. Chou, Int. J. Hydrogen Energy 38 (2013) 7307–7325.
[43] Y. Kobayashi, J. Horiguchi, S. Kobayashi, Y. Yamazaki, K. Omata, D. Nagao, M. Konno, M. Yamada, Appl. Catal. A: Gen. 395 (2011) 129–137.
[44] L. Li, S. Niu, Y. Qu, Q. Zhang, H. Li, Y. Li, W. Zhao, J. Shi, J. Mater. Chem. 22 (2012) 9263–9267.
[45] L.L. Xu, H.L. Song, L.J. Chou, Catal. Sci. Technol. 1 (2011) 1032–1042.
[46] C. Boissiere, D. Grosso, A. Chaumonnot, L. Nicole, C. Sanchez, Adv. Mater. 23 (2011) 599–623.
[47] D.P. Debecker, P.H. Mutin, Chem. Soc. Rev. 41 (2012) 3624–3650.
[48] T.Y. Kuo, S.C. Chen, W.C. Peng, Y.C. Lin, H.C. Lin, Thin Solid Films 519 (2011) 4940–4943.
[49] A.V. Neimark, P.I. Ravikovitch, Microporous Mesoporous Mater. 44–45 (2001) 697–707.
[50] A.V. Neimark, P.I. Ravikovitch, A. Vishnyakov, J. Phys.: Condens. Matter 15 (2003) 347–365.
[51] P.I. Ravikovitch, A.V. Neimark, J. Phys. Chem. B 105 (2001) 6817–6823.
[52] F. Jiao, H. Yen, G.S. Hutchings, B. Yonemoto, Q. Lua, F. Kleitz, J. Mater. Chem. A 2 (2014) 3065–3071.
[53] W. Wang, H.Y. Wang, W. Wei, Z.G. Xiao, Y. Wang, Chem. Eur. J. 17 (2011) 13461–13472.
[54] Z.R. Zhang, T.J. Pinnavaia, J. Am. Chem. Soc. 124 (2002) 12294–12301.
[55] A. Adeyemo, G. Hunter, P.K. Dutta, Sens. Actuators B 152 (2011) 307–315.
[56] R.L. Liu, Y.F. Shi, Y. Wan, Y. Meng, F.Q. Zhang, D. Gu, Z.X. Chen, B. Tu, D.Y. Zhao, J. Am. Chem. Soc. 128 (2006) 11652–11662.
[57] M. Kuemmel, D. Grosso, C. Boissière, B. Smarsly, T. Brezesinski, P.A. Albouy, H. Amenitsch, C. Sanchez, Angew. Chem. Int. Ed. 44 (2005) 4589–4592.
[58] Z.K. Zhao, R.H. Jin, Y. Li, Y.T. Dai, T. Muhammad, Catal. Sci. Technol. 3 (2013) 2130–2139.
[59] R. Kydd, D. Ferri, P. Hug, J. Scott, W.Y. Teoh, R. Amal, J. Catal. 277 (2011) 64–71.
[60] J. Sehested, S. Dahl, J. Jacobsen, J.R. Rostrup-Nielsen, J. Phys. Chem. B 109 (2005) 2432–2438.
[61] A.L. Kustov, A.M. Frey, K.E. Larsen, T. Johannessen, J.K. Nørskov, C.H. Christensen, Appl. Catal. A: Gen. 320 (2007) 98–104.
[62] G.D. Weatherbee, C.H. Bartholomew, J. Catal. 68 (1981) 67–76.
[63] T. Inui, M. Funabiki, M. Suehiro, T. Sezume, J. Chem. Soc. Faraday Trans. 1: Phys. Chem. Condens. Phases 75 (1979) 787–802.